Polymer 50 (2009) 5812–5823

Contents lists available at ScienceDirect

Polymer

journal homepage: www.elsevier.com/locate/polymer

Trichroic infrared analysis of the strain-induced structural changes in the PA6 layer of PA6/PE multilayer films under biaxial drawing

N. Sallem-Idrissi [a,b], V. Miri [a,*], S. Elkoun [a,1], P. Krawczak [b], M.-F. Lacrampe [b], J.-M. Lefebvre [a], R. Seguela [b,*]

[a] Université de Lille Nord de France-Centre National de la Recherche Scientifique, Université de Lille1, Laboratoire Structure et Propriétés de l'Etat Solide, Batiment C6, Cité Scientifique, 59655 Villeneuve d'Ascq, France

[b] Ecole des Mines de Douai, Département Technologie des Polymères et Composites, & Ingénierie Mécanique, 941 rue Charles Bourseul, 59508 Douai, France

ARTICLE INFO

Article history:
Received 25 June 2009
Received in revised form
31 August 2009
Accepted 18 September 2009
Available online 7 October 2009

Dedicated to the memory of Dr. Kenneth C. Cole, NRC-IMI, Boucherville, Canada.

Keywords:
Nylon6
Biaxial drawing
Trichroic infrared analysis

ABSTRACT

This work deals with the structural evolution under biaxial drawing of PA6/tie/PE multilayer films as a function of composition. The occurrence of plastic instabilities in the PA6 layer in the multilayers is strongly reduced with respect to the PA6 monolayer film and the maximum biaxial drawability of PA6 is considerably improved with increasing PE layer thickness. Quantitative evaluation by trichroic infrared analysis of the various crystal forms of the PA6 component shows that the strain-induced β–α crystalline phase transition is delayed in the multilayers, *i.e.* equivalent level of phase transformation is reached at higher strains. Similar phenomenon is observed regarding the orientation within the film plane of the PA6 chains in the strain-induced α-crystals, *i.e.* equivalent chain orientation is reached at higher strains in the multilayers. The deformation synergism between the PA6 and PE layers is discussed in terms of benefiting effect from the PE layer that prevents plastic instabilities and promotes homogeneous deformation accompanied with orthotropic extension of the chains in the PA6 layer. This is the driving force to the delay of the detrimental β–α phase transition of PA6, the mechanically anisotropic α-crystals being highly crack-prone in contrast to the ductile isotropic β-crystals. Film rupture is shown to occur when the PA6 strain-induced α-crystals reach a constant content of about 10%, irrespective of film composition and draw temperature in the range 80–110 °C. This kind of critical phenomenon is assigned to a percolation process of the crack-prone α-crystals.

1. Introduction

Coextrusion of different polymers into multilayer films is a rather conventional means for combining properties of several components into a single material and fulfilling optimum requirements in the field of mechanical, optical and gas-barrier properties. In parallel, biaxial drawing is largely used for improving mechanical performances of films such as tear and puncture resistance, and barrier properties as well. There is yet an actual challenge for applying this solid state process to multilayer materials for which the various components display different behavior and do not necessarily have the same optimum processing parameters.

Polyamide6, otherwise known as Nylon6, displays good thermo-mechanical properties together with chemical resistance and excellent barrier properties. However, oxygen permeability drastically increases in the presence of humidity. Besides, nylon6 exhibits rather poor ability for biaxial orientation. Only simultaneous biaxial drawing can be achieved in a narrow temperature window far below the melting point, and the strain at rupture remains low as compared with uniaxial drawing [1–3]. In contrast, the highly oxygen-permeable polyolefins such as polyethylene exhibit good barrier properties to water vapor. Moreover, biaxial orientation can be easily applied to polyolefins in a wide temperature range up to the melting point, in simultaneous or sequential modes.

The usual mechanical properties as well as the uniaxial and biaxial drawing behavior are strongly dependant on the processing conditions due to the significant impact on morphology, crystalline structure and texture, crystal content and molecular orientation. Polyethylene exclusively crystallizes in its stable orthorhombic form with little propensity for martensitic-like phase transition into a monoclinic form under strain. In contrast, nylon6 displays polymorphism that strongly depends on thermo-mechanical history [4]. The monoclinic α-phase is promoted by slow cooling from the melt, whereas the pseudo-hexagonal γ-phase develops under rapid cooling and/or high speed spinning. The mesomorphic β-phase is observed at room temperature after quenching of nylon6 from the melt. This thermodynamically unstable β-form transforms into the α-form upon thermal annealing and/or plastic drawing

* Corresponding authors.
E-mail addresses: valerie.miri@univ-lille1.fr (V. Miri), roland.seguela@univ-lille1.fr (R. Seguela).
[1] Present address: Département de Génie Mécanique, Université de Sherbrooke, Sherbrooke, Canada J1K 2R1.

0032-3861/$ – see front matter © 2009 Elsevier Ltd. All rights reserved.
doi:10.1016/j.polymer.2009.09.052

[5–7]. The γ-form, which is stable with regard to thermal annealing, undergoes a strain-induced phase transition into the α-form upon uniaxial drawing above 180 °C. The α-form is highly stable whatever the thermo-mechanical treatment [5–7] and is typically stiffer and less ductile than the β- and γ-forms, as can be judged from the higher modulus and yield stress, and the lower strain at break [8,9].

This paper deals with the biaxial drawing of polyethylene/tie-layer/nylon6 multilayer blown films. The structural evolutions of both the polyethylene and the nylon6 components of the multilayer films were investigated by means of infrared trichroic analysis and differential scanning calorimetry in order to get an insight into the plastic deformation processes of each component. This helps understand why and how the plastic behavior of the nylon6 component in the multilayer films is modified with respect to the monolayer parent polymer.

2. Experimental

2.1. Materials

The materials of the study were a linear low density polyethylene (LLDPE) and a low density polyethylene (LDPE), both purchased from SABIC. For processing reasons, the PE layer in the blown films consisted of a 30% LDPE/70% LLDPE blend. The polyamide6 (PA6) was provided by DSM (Geleen, The Netherland), as well as the linear low density polyethylene grafted with 0.16 mol% of maleic-anhydride (PE-*g*-MA) that was used as tie layer. The materials characteristics given in Table 1 were provided by the manufacturers. The molar weight data were determined from standard size exclusion chromatographic methods for polyethylene and polyamide 6.

2.2. Processing of the multilayer films

Prior to processing into films, the PA6 pellets were dried under vacuum for 24 h at 80 °C and a 30/70 mixture of LLDPE and LDPE pellets was prepared for extrusion of the PE layer. The PE/PE-*g*-MA/PA6 (internal-layer/tie-layer/external-layer) films have been manufactured on a 3-layer coextrusion-blowing die having an inner diameter of 120 mm and a die gap of 1.2 mm. More details on the tubular coextrusion line can be found elsewhere [10]. The total flow rate was held constant at 32 kg/h. The 3-layer films were blown through the annular die at 250 °C and subsequently cooled down with air at 4 °C. The blow-up and the take-up ratios were fixed at 1.2 and 20, respectively. Three different multilayer films were prepared by changing the PA6/PE layer thickness ratio via the flow rate of each component, the adhesive layer thickness and the overall thickness of the films being kept at the constant values 10 μm and 100 μm, respectively. The layer thickness was controlled by means of optical microscopy on cross-section slices. Monolayer films of PA6 and PE were produced using the same extrusion conditions. The three principal axes of the films are defined as the machine (MD) or take-up direction, the transverse (TD) or blow-up direction and the normal (ND) direction through the film thickness.

Table1
Molecular and physical characteristics of the raw materials: Number-average and weight-average molar weights, $M_n$and M_w; melt flow index, MFI; density, ρ.

Polymer	M_n (kDa)	M_w (kDa)	MFI[a] (g/10 min)	ρ (g/cm^3)
LLDPE	–	138	1.00	0.918
LDPE	–	374	0.85	0.921
PE-*g*-MA	–	92	2.70	0.928
PA6	25	50	–	1.13

[a] MFI measurements at 190 °C under 2.16 kg.

Table 2
Compositions of the multilayer as-blown films.

Films	Layer thickness (μm)[a]		
	PA6	PE-*g*-MA	PE
PE	–	–	100
25PA/65PE	25	10	65
45PA/45PE	45	10	45
60PA/30PE	60	10	30
PA	100	–	–

[a] measured from optical micrographs of film cross-sections; maximum thickness fluctuation = ±2 μm.

The films were dried under vacuum for three days at room temperature (RT) prior to any kind of investigation. Table 2 summarizes the film compositions and codes that account for PA6 and PE layer thicknesses.

2.3. Mechanical testing

Prior to drawing, the samples were annealed at the draw temperature for 5 min in order to stabilize the crystalline structure of the PA6 layer. Biaxial drawing experiments were carried out on a Cellier tenter frame consisting of four pantographs driven by two hydraulic jacks at right angle, and operated in a temperature-regulated oven. Force sensors allowed measuring the draw force in the two principal directions. Square specimens of gauge length 105 mm were submitted to simultaneous equibiaxial drawing at a constant jack speed of 60 mm/min, *i.e.* an initial strain rate of 10^{-2} s^{-1}. The engineering stress–strain curves were averaged from the data recorded in the two drawing directions, taking into account the friction contribution from the pantographs determined thanks to *blank* experiments without sample. The engineering strains are defined as $\epsilon_{eng} = \Delta L/L_0$ where L_0 is the gauge length and ΔL the macroscopic sample elongation assessed from the jack displacement. Considering that deformation may be heterogeneous in some cases, local strains $\epsilon = \Delta l/l_0$ were measured from 1×1 cm^2 square grids printed on the samples, l_0 and l being the mesh size prior and after drawing, respectively.

2.4. Thermal behavior

Differential Scanning Calorimetry (DSC) was carried out on a Perkin-Elmer DSC-7 apparatus. The 0–250 °C temperature range was calibrated using high purity indium and zinc samples, at the same heating rate of 10 °C/min used for the analysis of the polymer samples. At least five specimens of every sample were scanned for reproducibility. The crystal weight fraction of the PA6 and PE film components was determined using the values of 230 and 290 J/g for the melting enthalpy of 100% crystalline materials, respectively [11]. The mass of each component in the samples was computed from the sample mass and the layer thickness ratio. The melting point of the two components was taken at the peak of the melting endotherms.

2.5. X-ray scattering

Wide-angle X-ray scattering (WAXS) was carried out at RT in transmission mode. The Ni-filtered Cu-Kα radiation ($\lambda = 1.54$ Å) was generated by a Panalitical sealed tube operated at 40 kV and 20 mA. The WAXS patterns were recorded on imaging plates at a sample-to-film distance of 60 mm, using a 0.3 mm pinhole collimation.

2.6. Infrared spectroscopy

The Fourier Transform Infrared (FTIR) spectra were collected in transmission mode on a Perkin–Elmer 2000 spectrometer equipped

with a narrow range MCT detector and a gold wire polarizer. Every FTIR spectrum consisting of 130 scans was recorded over the wavenumber range 580–5200 cm^{-1} with a resolution of 2 cm^{-1}. The reduced absorbance is computed with respect to the layer thickness.

For characterizing the initial crystalline structure of the PA6 component and the strain-induced evolution, spectra were normalized with respect to the PA6 layer thickness and analyzed over the wavenumber range 850–1150 cm^{-1} where the absorption spectra of the various PA6 crystalline forms have been clearly identified in literature [12]. Furthermore, the PE absorption is extremely small in this wavenumber range. For the films having a PA6 layer thickness below 25 μm after biaxial drawing, the intensity of the characteristic bands was too low for accurate quantitative analyses. In that case, the measurements have been performed in the wavenumber range 1150–1330 cm^{-1} that is also free from PE absorption. Validation of this method was done by cross-checking data obtained from the two spectral domains for film samples having a 25 μm thick PA6 layer prior to drawing.

The PE component was investigated in the wavenumber range 750–700 cm^{-1} where no PA6 absorption band interferes with the selected PE bands.

Regarding isotropic as-blown films, the "structure factor" spectrum S_0 was calculated from the equation

$$S_0 = \frac{1}{3}(S_M + 2S_T) \tag{1}$$

where S_M and S_T hold for the spectra measured with the polarization parallel and perpendicular to the M and T directions, respectively.

In the case of biaxially drawn samples having 3D texturing, trichroic infrared measurements were required. Though not a novel investigation method [13–19], trichroic infrared analysis has never been used for quantitative purpose other than orientation assessment in spite of attractive potentiality and convenience. Absorbance measurements through the thickness were carried out by tilting the films about the T axis at 45° with respect to the IR beam, and the spectrum S_{MN} was measured with the polarization in the MN plane. Then, the S_N spectrum corresponding to a polarization through the thickness was computed from the following relation [13,17]

$$S_N = \left(2n^2\right)\sqrt{1-\frac{1}{2n^2}} \times S_{MN} - \left(2n^2-1\right) \times S_M \tag{2}$$

where n is the effective refractive index of the multilayer structure in the direction of the beam propagation. This parameter is calculated from the composition of the multilayer film and the refractive indices of PA6 and PE, taken to be 1.53 and 1.52, respectively [4,20]. The refractive indices of PE-*g*-MA and PE were taken equal. Then, the S_0 spectrum for biaxially drawn samples was calculated from the equation:

$$S_0 = \frac{1}{3}(S_M + S_T + S_N) \tag{3}$$

Based on the calculated S_0 spectra, a quantification of the crystalline phases as a function of strain was made using the same procedure as described in ref.[21]. The absence of absorption bands from the PE component in this wavenumber range was particularly convenient for the analysis. The 929, 952, 960 and 1030 cm^{-1} bands are assigned to the PA6 α-phase, whereas the 915 and 1000 cm^{-1} bands are ascribed to the PA6 γ-phase. Though the FTIR spectrum of the β-form does not display characteristic absorption bands, it can be perfectly distinguished from the α- and γ-form spectra. For quantifying the various crystalline phases, the S_0 spectra were fitted with a linear combination of spectra of the PA6 crystalline "pure phases" (experimental data files) having major α, β and γ-forms, over the wavenumber ranges 850–1150 cm^{-1} or 1150–1330 cm^{-1} depending on the PA6 film thickness. The so-called "pure phases" were prepared via specific chemical or thermal treatments described elsewhere [8,22,23]. The relative proportions of the three "pure phases" obeyed $\chi_\alpha + \chi_\beta + \chi_\gamma = 1$. The mean square deviation of the best spectrum fittings did not exceed 5%. The standard deviation on the χ_α, χ_β and χ_γ data have been estimated to about ±3%.

The orientation of a molecular axis i is usually described by three Herman's orientation functions f_{ij} where $j = M$, T or N holds for the directions defined above. The three orientation functions must obey the relationship

$$f_{iM} + f_{iT} + f_{iN} = 0 \tag{4}$$

If the transition moment of an infrared vibration is parallel to one of the i axes, the Herman's orientation function can be calculated by means of the following equation

$$f_{ij} = \frac{1}{2}\left(\frac{A_j}{A_0} - 1\right) \tag{5}$$

where A_j and A_0 are the band intensities in the S_j and S_0 spectra, respectively.

The 929 and 834 cm^{-1} bands were used to assess the α phase orientation in the PA6 layer [13,17]. The 929 cm^{-1} band is assigned to a vibration mode having its transition moment along the molecular chain axis (*c*-axis), whereas the transition moment of the 834 cm^{-1} mode is along the H-bonded sheets normal (*b*-axis). It is to be noticed that the *b*-axis is not a crystallographic axis. For a given j direction, the orientation of the H-bonds, *i.e.* the *a*-axis normal to the b-c plane, is computed from

$$f_{aj} + f_{bj} + f_{cj} = 0 \tag{6}$$

The f_{aj} and f_{bj} orientation functions of the orthorhombic crystalline phase of PE has been computed from the analysis of the 730 and 720 cm^{-1} bands for which the transition moment is respectively parallel to the *a*- and *b*-axes of the unit cell [24]. The f_{cj} orientation function of the *c*-axis was then deduced from the f_{aj} and f_{bj} orientation functions using Eq. (6).

2.7. Atomic force microscopy

Topographic AFM observations (height images) were performed on a Dimension 3100 apparatus from Digital Instruments operated in light Tapping Mode, using a set-point amplitude ratio close to 0.9 in order to reduce indentation effects and thereby optimize the topographic contrast. The Nanoworld silicon SPM sensors (type NCL) had a tip radius less than 10 nm, the nominal spring constant and resonance frequency of the cantilever being respectively 48 Nm^{-1} and 190 kHz [25].

3. Results and discussion

3.1. Structural behavior of the blow films

The through-view WAXS patterns of Fig. 1 show uniform scattering rings for all the blown films. The absence of crystalline texturing, in spite of large difference in the take-up and blow-up ratios, is relevant to very low stresses in the films at the very moment crystallization took place during the blow-extrusion process. The overlap of the PE and PA6 scatterings does not allow determining the PA6 crystalline structure, more particularly regarding the main (001) reflection of the PA6 γ-crystal form and the (110) reflection of the PE orthorhombic crystal that both appear at a scattering angle $2\theta \approx 21°$. Nevertheless, the characteristic

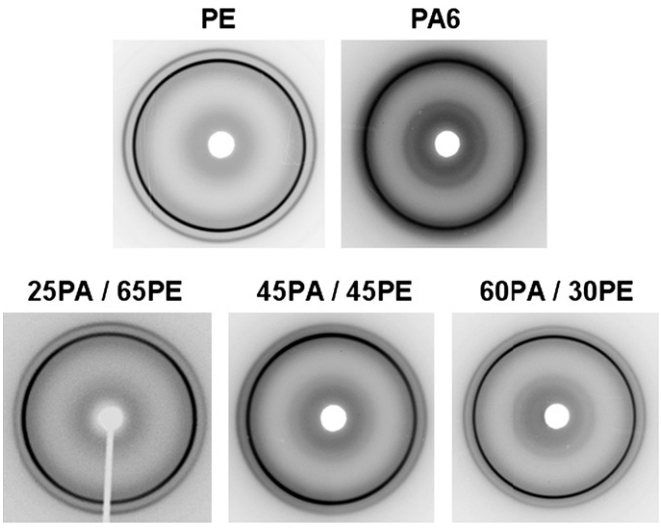

Fig. 1. Through-view WAXS patterns of the as-blown films.

γ-crystal scattering of the PA6 monolayer film that is commonly observed in nylon6 spun fibers [23] is relevant to a fast cooling but not to an actual quenching of the film during the blowing process.

The FTIR experiments provide additional information on the texturing of the as-blown films. Fig. 2 shows the polarized spectra of both the PA6 and PE monolayer films for the three main directions M, T, N. The great similarity of the three spectra of the PA6 film is indicative of nearly perfect isotropy, within experimental accuracy. This means that the PA6 chains were able to completely relax during extrusion-blowing. On the contrary, the S_N spectrum of the PE film is quite different from the S_M and S_T spectra. This means that

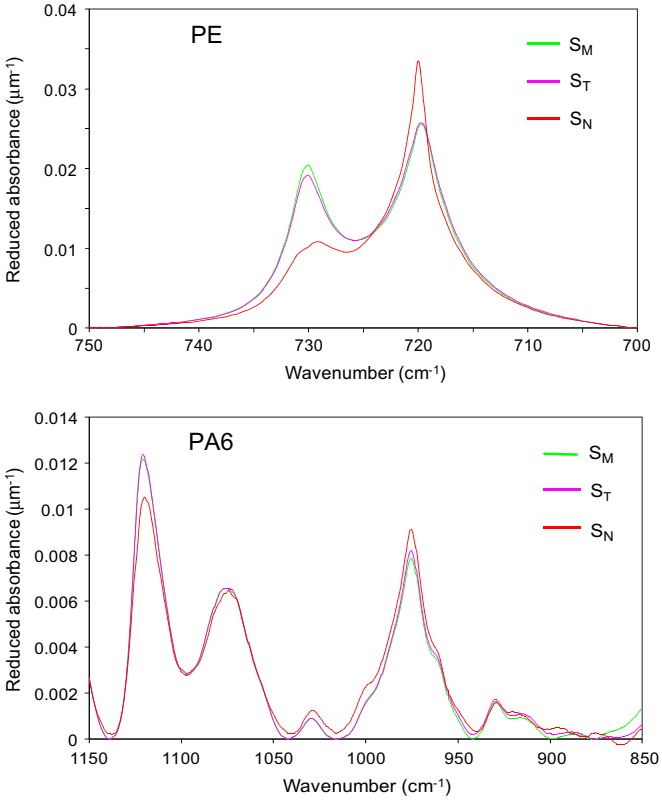

Fig. 2. Polarized spectra of the PA6 and PE monolayer films.

substantial planar chain orientation induced by the process has been retained prior to crystallization. This is relevant to the higher viscosity of the PE component with respect to the PA6 due to much higher molar weight of the former component. The three multilayer films also displayed structural isotropy of the PA6 layer and slight orthotropy for the PE layer.

Further analysis of the FTIR spectra give better insight into the structural habits of the PA6 component of the various films and quantitative assessment of the crystalline forms. The experimental spectrum of the 45PA/45PE multilayer film in the wavenumber range 850–1150 cm^{-1} is reported in Fig. 3a together with the spectrum computed from the best fitting linear combination of the experimental "pure" component spectra of the three PA6 crystal forms shown in Fig. 3b. The optimized computation gives the $\chi_\alpha \approx 0\%$, $\chi_\beta \approx 87\%$, and $\chi_\gamma \approx 13\%$. The missing of the characteristic α-PA6 bands in Fig. 3a supports the computation of $\chi_\alpha \approx 0\%$. The predominance of the β-form with little amount of γ-crystals confirms that the cooling rate was high enough for preventing formation of the α phase, in agreement with Kyotani and Mitsuhashi [26] study of nylon6 crystallization kinetics. Moreover, the very good matching of the computed and experimental spectra, over the whole wavenumber range of Fig. 3a, gives confidence to the computation procedure.

Fig. 4 shows an example of the FTIR analysis of the PA6 component in the wavenumber range 1150–1325 cm^{-1}, in the case of the 25PA/65PE film. The linear combination for the optimized computed spectrum results in the following crystal contents: $\chi_\alpha \approx 0\%$, $\chi_\beta \approx 81\%$, and $\chi_\gamma \approx 19\%$. Again, the β-form of PA6 is predominant, with no α-form crystals.

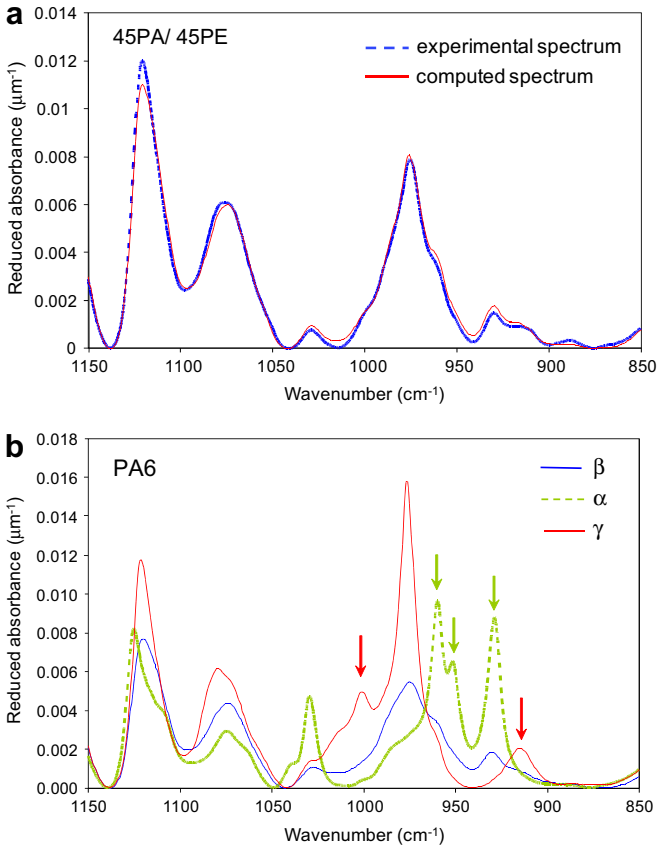

Fig. 3. FTIR analysis of the PA6 component in the spectral range 850–1150 cm−1: (a) experimental and computed structure factors for the 45PA/45PE film. (b) experimental structure factors of the 3 "pure component" crystal forms of PA6 used in the linear combination fitting.

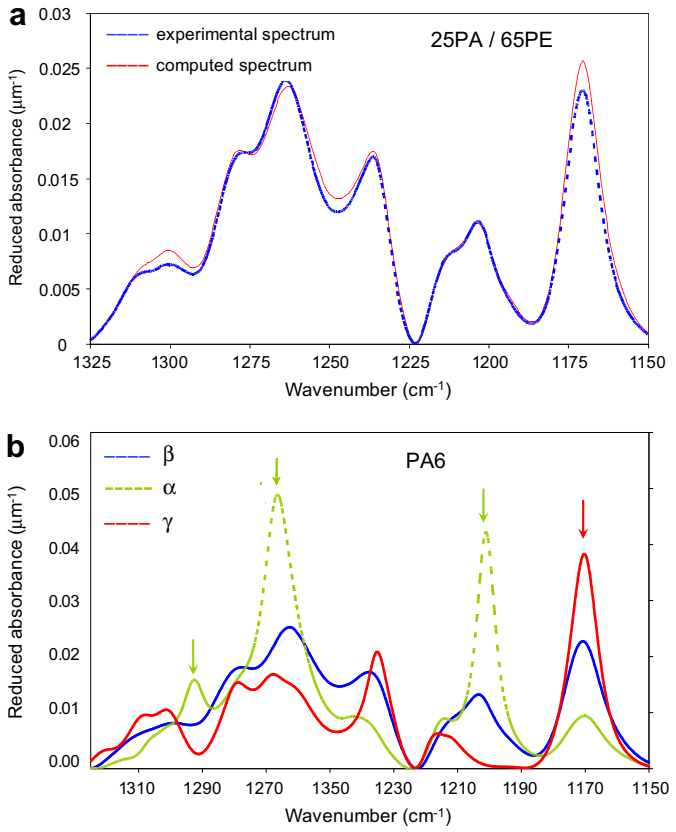

Fig. 4. FTIR analysis of PA6 component in the spectral range 1150–1310 cm−1: (a) experimental and computed structure factors for the 25PA/65PE film; (b) experimental structure factors of the 3 "pure component" crystal forms of PA6 used in the linear combination fitting.

All the quantitative data regarding the PA6 crystalline forms are reported in Table 3. These data clearly show that PA6 crystallizes in predominant β-form with minor presence of γ-form crystals, the β-form content being little depends on the film composition.

The DSC heating curves of the monolayer and multilayer films reported in Fig. 5 display two endotherms respectively assigned to the melting of the PE and PA6 layers. The endotherm in the range 200–225 °C is relevant to the melting of PA6 α-crystals issued from the thermally induced reorganization of the original mesomorphic β-species of the PA6 component into stable α-crystals, according to previous studies on PA6 cast films [8,21]. This reorganization process is clearly disclosed by the broad endotherm in the 100–180 °C range of the DSC trace of the neat PA6 film. The broadness of the process make it undetectable in the case of the multilayer films. The hump at about 210 °C on the main peak is indicative of the melting of thermodynamically stable PA6 γ-crystals. The faint exotherm at about 190 °C on the DSC traces of the monolayer and multilayer films can be ascribed to the melting and quick recrystallization into α-crystals of some unstable γ-crystals, as already shown by several authors regarding nylon6 [27–29] and nylon12 [30] as well.

Table 3
Composition of the various crystalline forms in the PA6 layer of the as-blown films: α form, χ_α; β form, χ_β; γ form, χ_γ.

Films	χ_α (%)	χ_β (%)	χ_γ (%)
25PA/65PE	0	85	15
45PA/45PE	0	87	13
60PA/30PE	0	83	17
PA	0	85	15

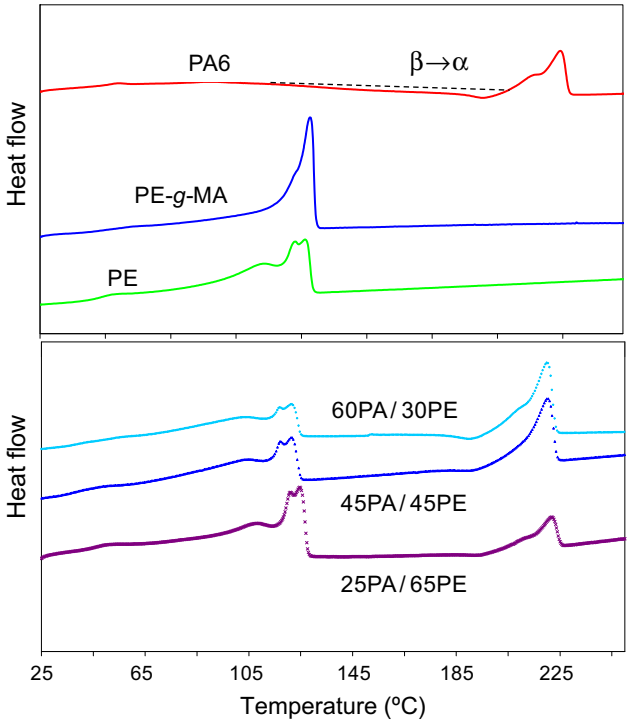

Fig. 5. DSC heating scans of the as-blown films.

The absence of a cold-crystallization exotherm above the glass transition temperature of the PA6 component, *i.e.* about 50 °C (see the neat PA6 curve of Fig.5), gives evidence that no additional PA6 crystalline phase is generated from the amorphous PA6 phase during the heating scan. This is an indication that the PA6 layer did not suffer from chain immobilization during the solidification process after blow-extrusion, in contrast to cast-extrusion that is well known to partly prevent optimum ordering [8,31,32]. One may thus assume that the α-crystal content computed from the melting endotherm of the PA6 component is identical to that of the β-crystals from which they are issued in the initial blown films, owing to the β–α transition during the DSC scan.

Regarding the melting endotherm of the PE layer in the range $30 < T < 125$ °C, the double peak at about 115 and 120 °C is relevant to a double crystallite size population, a typical feature of Ziegler–Natta LLDPE copolymers due to double distribution of co-units in the linear copolymer chains [33–35]. The broad peak ranging from 30 °C to 105 °C results from the melting of a mixture of long-branched chains and co-unit rich linear chains from the LDPE and LLDPE components, respectively. For comparison, the DSC heating trace of the PE-*g*-MA tie-component is also reported in Fig. 5. The melting endotherm typical of a low density polyethylene stands in the same temperature range as that of the PE layer blend.

Table 4 summarizes the main thermal characteristics of blown films. Whatever the multilayer film composition the melting point of the PE and PA layer are close to those measured on the monolayer films within the standard deviation of the experimental data. In contrast, the crystallinity index of the PE layer seems to slightly increase with decreasing layer thickness, whereas that of the PA6 layer is roughly constant within the experimental accuracy. It is to be noticed that the X_c data of the PE component which include the contribution of the PE-*g*-MA tie layer are somewhat higher than the X_c values of the pure PE and PE-*g*-MA constituents. This may be an artifact due to the heat capacity jump from the PA6 glass transition at about 50 °C that introduces an overestimation of the melting enthalpy.

Table 4
Thermal characteristics of the multilayer as-blown films: fusion temperature, Tf; crystal weight fraction, Xc.

Films	Tf PA6 (°C)	Xc PA6 (%)	Tf PE (°C)[b]	Xc PE (%)[a]
PE	–	–	121	40 ± 5
25PA/65PE	219	28 ± 3	122	44 ± 3
45PA/45PE	220	28 ± 3	122	47 ± 7
60PA/30PE	220	28 ± 3	122	52 ± 5
PA	223	25 ± 3	–	–

[a] Xc PE is a global measurement for the PE and PE-*g*-MA layers due to the impossibility of resolving the respective melting curves of the two components on the DSC traces.
[b] Tf PE is determined from the upper peak of the bimodal endotherm.

The optical micrographs of Fig. 6a show that the morphology of both the PE and PA6 layers is rather uniform through the film thickness. The measured layer thicknesses are quite consistent with the values predicted from the flow rates of the two components during extrusion (Table 2). No spherulitic structure could be observed in the PE layer at the resolution scale of the optical micrographs. Topographic AFM images as well did not reveal spherulites on the surface of the PE layer at a 10 μm scale. However, the PA6 layer displayed a well developed spherulitic structure at a 25 μm scale, as shown in Fig. 6b. Besides, the size of the PA6 spherulites is roughly similar in the monolayer and the multilayer films. Considering the invariance of the PA6 crystallinity index, this observation suggests no nucleation-induced effect from the PE-*g*-MA tie layer that could be suspected due to the chemical bonding of the PA6 chain ends on the MA units in the multilayers.

3.2. Mechanical behavior

Engineering stress–strain curves upon simultaneous equibiaxial drawing at $T_d = 100\ ^\circ C$ are reported in Fig. 7 for the PA6/PE multilayer film and the individual components. This figure reveals a gradual change from the PA6 to the PE monolayer film behavior with increasing PE content. Within the experimental accuracy, the stress–strain behavior of the multilayer films roughly obeys an additive mixture law of the components. Regarding both the yield stress and flow stress, the additive mixture law could have been anticipated in consideration of the *parallel* mechanical coupling of the two layers with respect to the tensile axis that *a priori* involves a uniform strain distribution, *i.e.* a *Voigt* mechanical coupling model [36]. The fact that a similar law applies to the strain at break is yet quite unexpected. Indeed, this means that the PA6 component can be drawn far beyond its capabilities of drawing alone. It is to be noticed that this surprising behavior is not just a question of layer thickness since monolayer PA6 films below 100 μm display the same stress–strain curve as that of Fig.7. Similar departure in the mechanical behavior of the monolayer and the multilayer films has been observed for all draw temperatures in the range 80–110 °C.

Another conspicuous aspect of the macroscopic mechanical behavior upon equibiaxial drawing is the quite uniform plastic deformation of the multilayer films which contrasts with the highly heterogeneous plastic deformation of the PA6 monolayer film which displays multiple necking in the early stages of drawing. The topographic AFM images of Fig. 8 give insight into the morphological changes at the scale of the films as a function of local biaxial

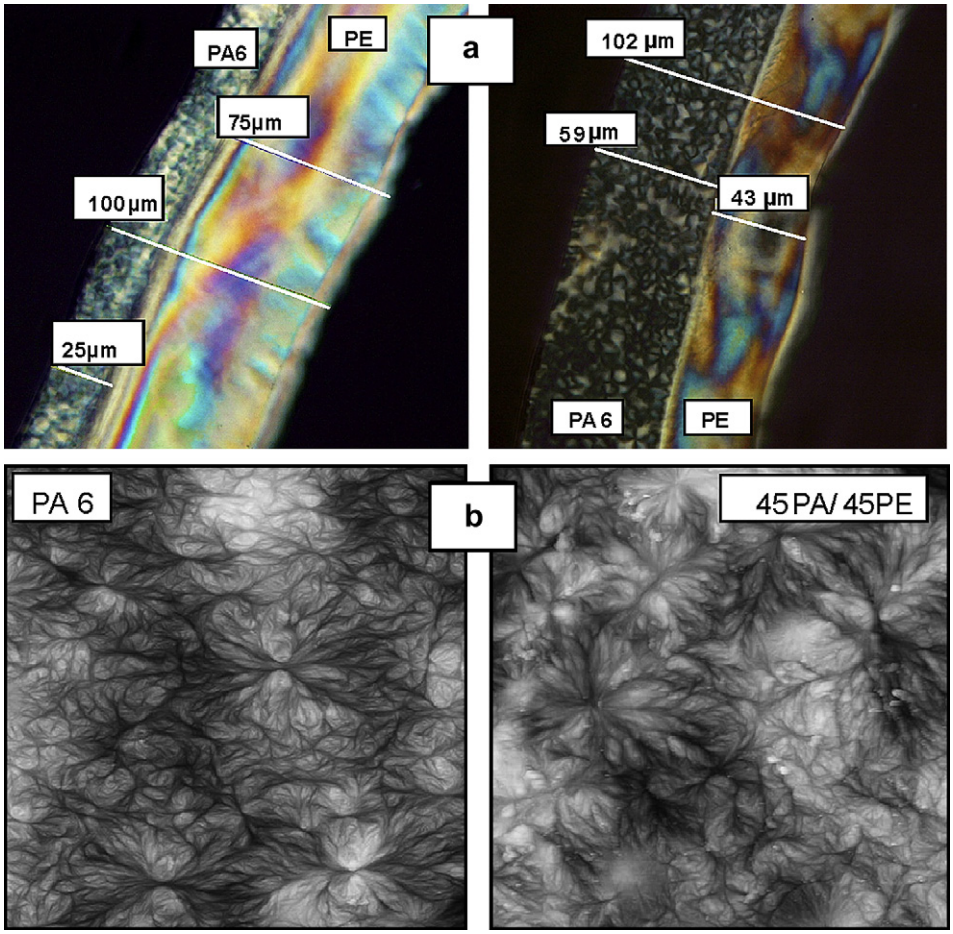

Fig. 6. (a) Light-polarized optical micrographs from cross-section slices of the 25PA/65PE and 60PA/30PE multilayer films (the PE-g-MA tie layer is undistinguishable from the PE layer); (b) Topographic AFM images ($25 \times 25\ \mu m^2$) of the free surface of the PA6 layer in the PA6 monolayer and the 45PA/45PE multilayer films.

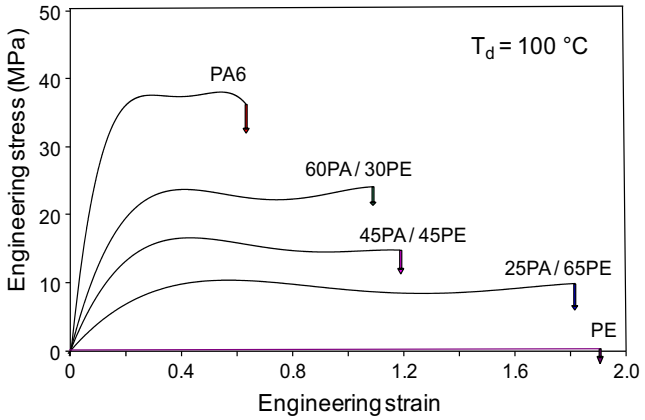

Fig. 7. Engineering stress–strain curves at $T_d = 100$ °C for the simultaneous equibiaxial drawing of the PA6 monolayer and the PA6/PE multilayer films.

strain. The darkening of the spherulite cores as strain increases is relevant to a lowering of the core surface level with regard to the periphery. This means that the plastic deformation is heterogeneous at the spherulitic size scale, the core region being the locus of higher plastic strains than the spherulite periphery. This heterogeneity is yet not the same for the various films as revealed by the different darkness contrast of the PA6 and 45PA/45PE films at equivalent biaxial strain.

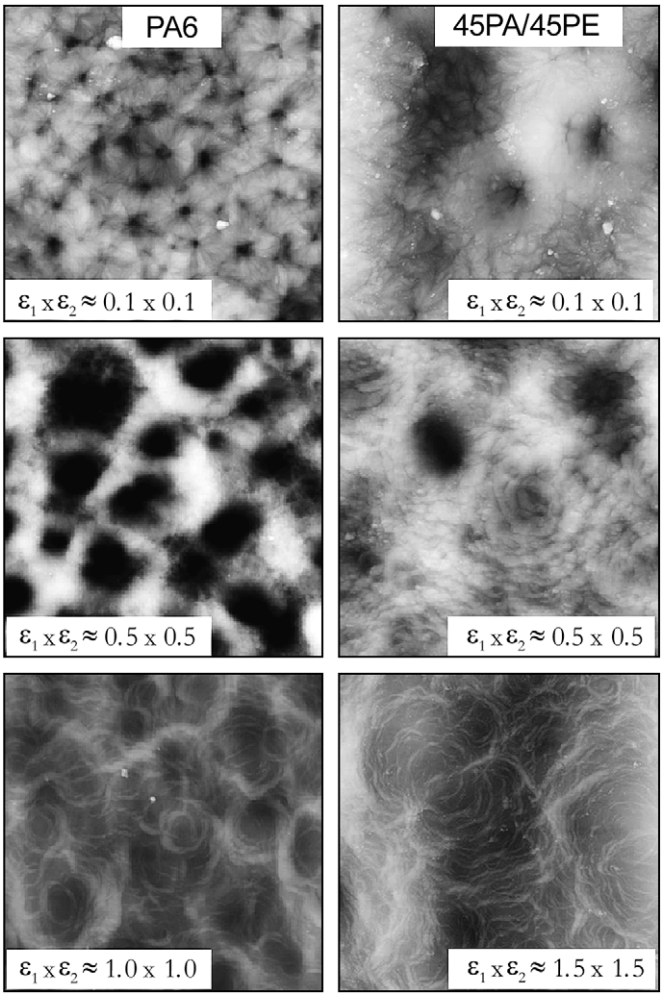

Fig. 8. Topographic AFM images of PA and 45PA/45PE films after equibiaxial drawing at $T_d = 110$ °C for various strains (image size = 25 × 25 μm^2; Z range = 2000 nm).

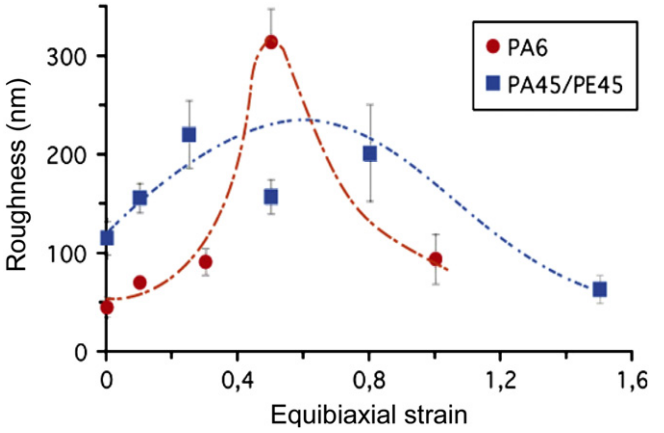

Fig. 9. Roughness profiles from AFM images of the PA6 monolayer and 45PA/45PE multilayer films as a function of equibiaxial strain (average roughness data over 25 × 25 μm images).

The roughness versus strain curves of Fig. 9 show a quite moderate increase by 2-fold of the surface relief for the 45PA/45PE multilayer whereas the PA6 monolayer displays a 6-fold roughness upswing for $\epsilon_1 \times \epsilon_2 \approx 0.5 \times 0.5$, before surface smoothing at large strains. This suggests that the PE layer promotes homogeneous plastic deformation of the PA6 component in the multilayer film. It is worth noticing that the maximum local plastic strain is noticeably greater than the engineering strain at rupture (Fig.7) for the PA6 monolayer, which is an additional hint of the high deformation heterogeneity. The capacity of the multilayer film to hinder plastic deformation localization in the PA6 layer at the spherulite scale is obviously a favorable factor for preventing the occurrence of plastic instabilities at the macroscopic scale.

These experimental findings regarding the structural aspects of the deformation at the macroscopic and mesoscopic scales are clear evidences that the plastic deformation mechanisms in the unlike layers of the multilayer films are somewhat different from those of the pure components, more particularly regarding the PA6 layer which exhibits drastically improved ductility.

Fig. 10 reports the equibiaxial strain at break for all the monolayer and multilayer films for the various draw temperatures in the range 80–110 °C. All the multilayer films exhibit simultaneous rupture of the PE and PA6 layer, without layer separation. The drawability of the PA6 layer in the multilayer films is gradually increased beyond that of the PA6 monolayer film in parallel with the thickness increase of the

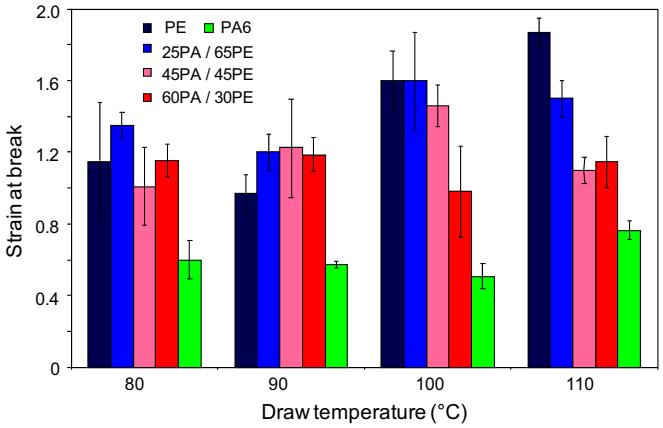

Fig. 10. Strain at break versus draw temperature for the various films.

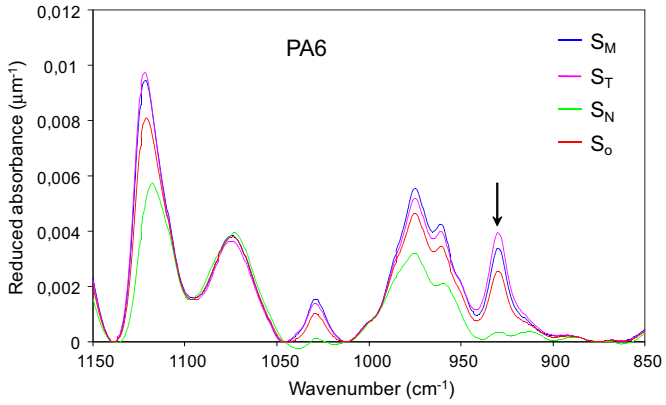

Fig. 11. Example of S_0 structure factor reconstruction from the S_M, S_N, and S_T polarized spectra for the PA6 monolayer film biaxially drawn $\varepsilon 1 \times \varepsilon 2 \approx 0.7 \times 0.7$ at $T_d = 90\,^{\circ}C$.

PE layer. For $T_d = 90\,^{\circ}C$ the drawability of the multilayers may be even improved beyond that of the two components, indicating a mechanical synergism between the unlike components instead of just a mixture law behavior. Notwithstanding, regarding the overall drawability of the multilayers, $T_d = 100$–$110\,^{\circ}C$ is the optimum temperature domain for biaxial drawing of the multilayers, as already reported for nylon6 [37,38]. This optimum results from a competition between two temperature-dependent phenomena in the PA6 component: (1) the thermal activation of the plastic processes and (2) the propensity for crack generation through the anisotropic H-bonded sheets. At $T_d > 110\,^{\circ}C$, the collapse of the paraffin-like inter-sheet interactions of the α-crystals turns the H-bonded sheets into a highly crack-prone structure, erasing any benefiting effect of temperature increase on plasticity.

3.3. Strain-induced structural evolution

Fig. 11 shows an example of FTIR structure factor computing from the three polarized spectra recorded for the principal directions of the PA6 monolayer film biaxially drawn up to $\varepsilon_1 \times \varepsilon_2 \approx 0.7 \times 0.7$ at $T_d = 90\,^{\circ}C$. The slight dissimilarity of the S_M and S_T spectra is relevant to not perfectly balanced biaxial strains. Indeed, due to the numerous plastic instabilities that develop in PA6 monolayer, well balanced sample pieces are very scarce. However, the very different S_N spectrum reveals both the structural orthotropy of the film sample and the strong texturing of the α-form as indicated by the global drop of the spectrum intensity and the disappearance of the 929 cm^{-1} band, respectively. The evolution of the structure factor S_0 as a result of biaxial drawing at $T_d = 90\,^{\circ}C$ is illustrated in Fig. 12 for the 45PA/45PE and 25PA/65PE films, in the wavenumber ranges 850–1150 and 1150–1310 cm^{-1}, respectively. Both films exhibit decreasing intensity of the bands assigned to the γ- and β-forms and increasing intensity of the α-form bands that are relevant to the growth of strain-induced α-crystals at the expense of β- and γ- crystal species.

The PA6 crystal phase changes with equibiaxial drawing were quantitatively assessed from the structure factor analysis into "pure" crystal form contributions. The data regarding the monolayer and multilayer films at $T_d = 90\,^{\circ}C$ are reported in Fig. 13. The γ-crystals gradually disappear at low ϵ values in parallel with the growth of α-crystals, for all films. Then the β-phase content monotonically drops for $\epsilon > 0.5$, whereas α-crystals continue growing till breaking. The major difference in structural evolution of the various films is the gradient of the strain-induced transition for $\epsilon > 0.5$: the lower the PA6 layer thickness, the lower the transition gradient (Fig. 13). In contrast, a major structural similarity of the various films is the limiting values of the β- and α-crystal contents at break, *i.e.* $\chi_\beta \approx 70\%$ and $\chi_\alpha \approx 30\%$.

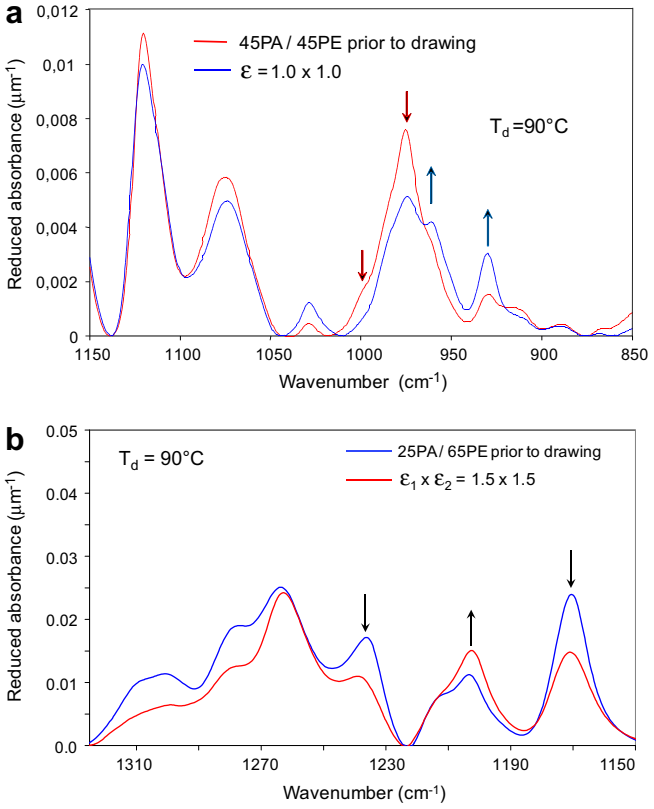

Fig. 12. Structure factors of the PA6 component of (a) the 45PA/45PE and (b) the 25PA/65PE films prior to drawing and after equibiaxial drawing at $T_d = 90\,^{\circ}C$.

It is worth noticing that the early disappearance of γ-crystals with constant χ_β for $\varepsilon < 0.5$ is not necessarily relevant to a direct γ-α phase transition. The γ-crystals may first turn disordered into β-form whereas the original β-crystals transform into α-form since the onset of drawing, leading to a global invariance of χ_β in the first stage of the biaxial drawing.

Fig. 14 reports the crystalline phase changes in the PA6 component as a function of equibiaxial strain at $T_d = 110\,^{\circ}C$ for the monolayer and multilayer films. The evolution of the crystal species is very similar to the case at $T_d = 90\,^{\circ}C$ (Fig. 13). Within the standard deviation of the data, the limiting values of the β- and α-crystal contents at break are identical for both temperatures, *i.e.* $\chi_\beta \approx 70\%$ and $\chi_\alpha \approx 30\%$.

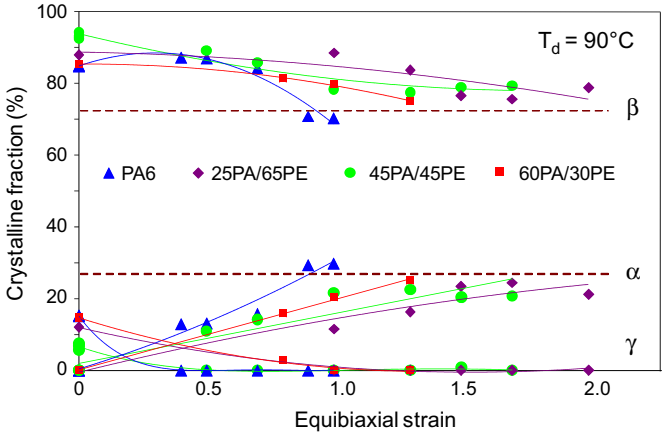

Fig. 13. Relative contents of the α-, β- and γ-crystal forms in the PA6 component versus strain for equibiaxial drawing at $T_d = 90\,^{\circ}C$ of the monolayer and multilayer films.

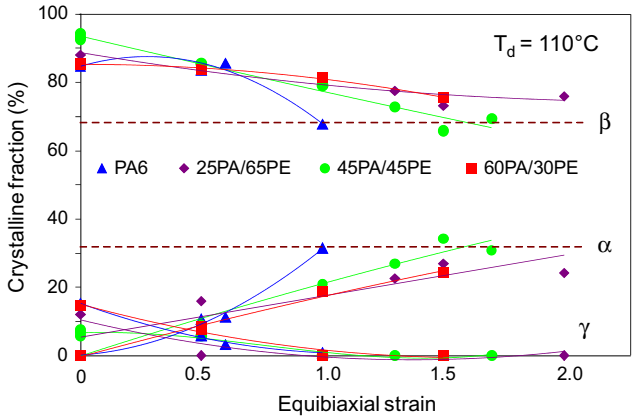

Fig. 14. Relative contents of the α-, β- and γ-crystal forms in the PA6 component versus strain for equibiaxial drawing at $T_d = 110\,^{\circ}C$ of the monolayer and multilayer films.

Valuable qualitative information on the mechanism of the phase changes can be gained from the WAXS analysis of the biaxially oriented films. Fig. 15 reports the 2D-patterns recorded for the PE, PA6 and 60PA/30PE films biaxially drawn at $T_d = 110\,^{\circ}C$ up to $\epsilon_1 \times \epsilon_2 \approx 1.0 \times 1.0$. At first sight, the patterns from the multilayer films roughly look like simple superposition of the patterns from the two parent component films, in both the through and edge-views. This means that the structural evolution of the two components in the multilayer films is not radically different from that of the individual parent films, on a qualitative standpoint. A more precise examination of the through-view patterns reveals fairly uniform scattering rings for all films that are relevant to an axial symmetry of the crystalline structure about the film normal consecutively to the equilibrated biaxial drawing. In contrast, the edge-view patterns exhibit more or less pronounced crystallographic texturing of the two components. Focusing first on the PE component, the two main reflections of the orthorhombic crystal form are present in the PE monolayer film. However, the slight anisotropy of the outer (200) reflection in the edge-view reveals a trend of PE crystalline texturing, the denser (200) planes having a preferred orientation parallel to the film surface. A similar behavior of the PE component can be observed for the 60PA/30PE multilayer film. This quite moderate PE texturing is due to the melting of a large part of this component during the biaxial drawing that allows molecular relaxation, so that the recrystallization of the molten part takes place in the isotropic state during the post-drawing cooling.

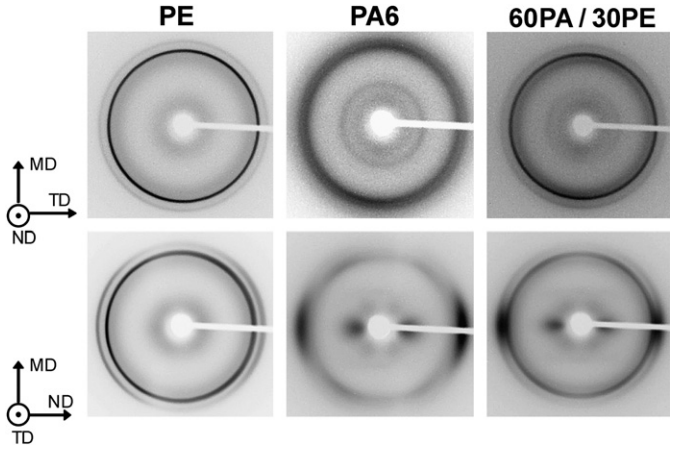

Fig. 15. Through-view (ND) and edge-view (TD) WAXS patterns of the PE, PA6 and 60PA/30PE films for an equibiaxial strain $\varepsilon_1 \times \varepsilon_2 \approx 1.0 \times 1.0$ at $T_d = 110\,^{\circ}C$.

Regarding PA6 in both the neat PA6 film and the 60PA/30PE film, the through-view patterns display a broad scattering ring indicative of the predominance of the mesomorphic β-phase. In contrast, the edge-view pattern reveals a strong (200) reflection of the PA6 α-form in equatorial position together with the (002) reflection in quadrant position. This is relevant to the orientation of the (200) crystallographic planes in the film plane, as observed in previous study of PA6 biaxial drawing [32,37]. It is worth noticing that this texturing is concomitant to the β–α phase transition, since no trace of the α-form can be seen in the through-view patterns. It must also be noticed that the (200) planes are the ones containing the H-bonds in the sheet-like structure of the PA6 α-form. This preferred planar texturing results, on the one hand, from the orientation of the most plastically compliant plane family within the film plane that undergoes shear deformation and, on the other, from the fact that the H-bonded planes in the PA6 α-form are the most compliant ones with regard to plastic shear (see ref. [39] and the discussion in ref.[37]).

Strictly similar texturing of the PE and PA6 layers have been observed for the 45PA/45PE and 25PA/65PE films.

The FTIR trichroic analysis provides better insight into the PA6 orientational behavior. Fig. 16 displays the Wilchinski diagrams of the orientation functions of the crystallographic axes of the α-form in the PA6 component as a function of equibiaxial strain at $T_d = 110\,^{\circ}C$ for the 45PA/45PE multilayer and the monolayer films. Indeed, only the PA6 α-form arising from the strain-induced β–α transition could be investigated owing to its clearly identified vibration modes, the γ-form being of little interest considering its disappearance for

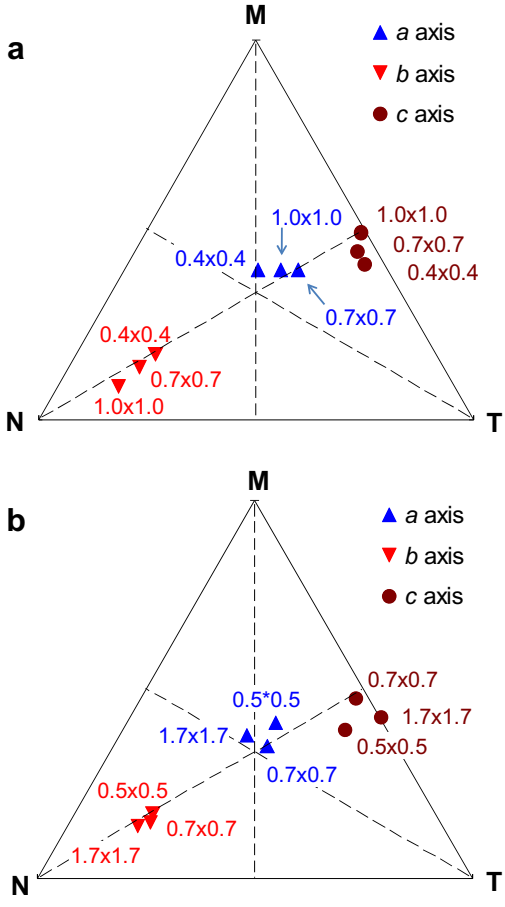

Fig. 16. Wilchinski diagrams of the f_{ij} orientation functions of the PA6 α-crystal in (a) the PA6 monolayer and (b) the 45PA/45PE multilayer films after equibiaxial drawing at $T_d = 110\,^{\circ}C$ (the numbers attached to the experimental points refer to the equibiaxial strain values).

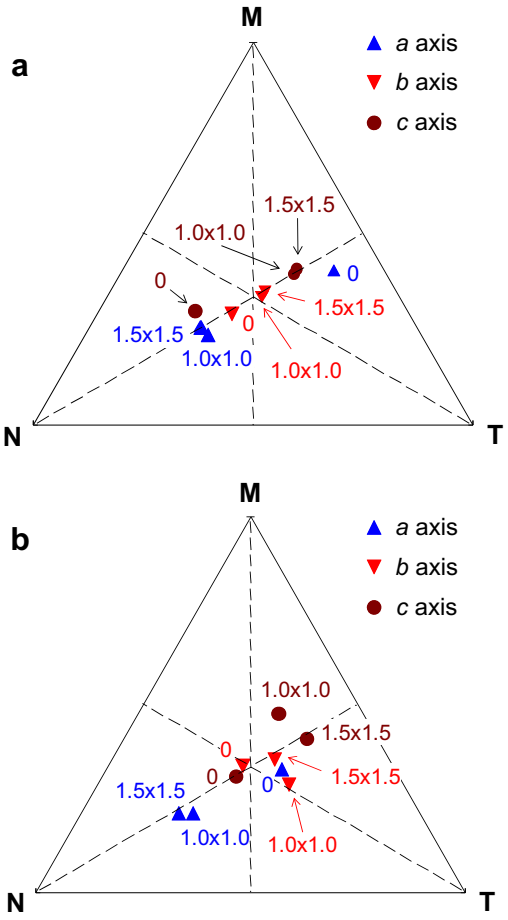

Fig. 17. Wilchinski diagrams of the f_{ij} orientation functions of the PE orthorhombic unit cell for (a) the PE monolayer and (b) the 45PA/45PE multilayer films after equibiaxial drawing at $T_d = 110\ ^\circ C$ (the numbers attached to the experimental points refer to the equibiaxial strain values).

$\varepsilon > 0.5$. The *b*-axis that is normal to the H-bonded sheets of the PA6 α-unit cell shows an orientation trend towards the N direction indicating that the sheets align parallel to the plane of the films, for both the monolayer and multilayer films. This is confirmed by the orientation of the *c*-axis (*i.e.* chain axis) in the MT plane. The orientation functions only slightly change with increasing strain, indicating that the α-form texturing is concomitant with the strain-induced β–α transition, *i.e.* when every α-crystal grows from an original β-form domain, the chain stretching directly draws the H-bonded sheets in the film plane. This is consistent with a previous observation by confocal Raman microspectroscopy that the β–α transition parallels the fibrillar transformation in PA6 β-spherulites under uniaxial drawing [40]. The slight data dispersion about the MT median is indicative that biaxial drawing is not perfectly equilibrated. It is however worth noticing that the crystalline orientation of the PA6 component is less pronounced in the multilayer film than in the monolayer parent, at equivalent strain. This is an evidence that strain-induced orientation of the PA6 chains in the MT plane is delayed for the multilayer film.

Regarding the PE component, the data of Fig. 17 show that the orientational behavior of the 3 crystal axes in the 45PA/45PE multilayer film can be hardly distinguished from that of the monolayer film at equivalent strain. Besides, the crystal chain axis is significantly less oriented in the MT plane than in the PA6 counterpart at similar strain (Fig. 16). This finding corroborates the previous WAXS data of Fig. 15 indicating low texturing in the PE layer due to partial melting and significant chain relaxation during biaxial drawing. This relaxation behavior of PE during biaxial drawing contrasts with the restricted relaxation observed after extrusion-blowing. The main reason lies in the difference in the duration of the two processes: indeed, 2–3 min are required for biaxial drawing up to break at 110 °C, the material being not thoroughly but largely molten, whereas the time elapsed between the die and the freezing line during the film extrusion-blowing was only 10–30 s at 280 °C, depending on the film type, the material being completely molten is this case.

4. Data analysis and discussion

The modification of the biaxial drawing behavior of PA6 in the multilayer films with respect to the monolayer film is directly connected with the inhibition of plastic instabilities, *i.e.* local regions of highly anisotropic plastic strain that do occur in neat PA6. The deformation of the multilayer films is much more uniform than that of the monolayer film at similar equibiaxial strain. This has direct incidence of the strain-induced structural changes since the orthotropic unfolding of the polymer coils in the film plane is not favorable to the β–α phase transition that requires both chain extension into planar conformation and perfect chain alignment. Orthotropic chain unfolding refrains chain alignment and therefore delays the β–α transition.

The presence of the PE companion layer is obviously the factor that reduces the PA6 trend for plastic instability and promotes homogenous plastic deformation under equibiaxial drawing. The additive mixture law of the tensile stress–strain curves of the two components that applies to the multilayer films is relevant to a parallel mechanical coupling of the two layers with respect to the applied stress. This surprisingly suggests a very weak incidence of the various components on the individual behavior of each other. The very minor changes in the PE structural behavior in the multilayers with regard to the monolayer film supports this assumption. Notwithstanding, the mechanical coupling of the unlike layers proved to be efficient to prevent necking in the PA6 layer and impart modifications in the structural and orientational behavior of the PA6 layer of the multilayer films with regard to the monolayer film for strains $\epsilon > 0.5$. This particular property of the PE layer on the PA6 mechanical behavior may be explained by the minute stress drop at yield of PA6 that generates necking, according to previous studies of uniaxial drawing in the same temperature range as in this work [37,38]. In the present instance, the viscous forces from the partially molten PE and tie layers are indeed suspected to be able preventing initiation of plastic instabilities in the PA6 layer, due in particular to the well known strain-hardening of LDPE elongational viscosity in the melt [41,42]. Besides, the viscosity and stiffness of the PE layer close to the interface should be enhanced owing to the covalent bonding to the PA6 chains via the PE-*g*-MA tie layer, if one assumes high compatibility of the PE-*g*-MA and PE components. Indeed, the anchoring to the PA6 layer of the PE-*g*-MA chains having 5 MA unit/chain in average is likely to involve a "crosslinking" effect of the PE layer at the interface, which in turn will provide additional strain-hardening. The PE layer should thus act as a "deformation guide" hindering plastic instabilities in the PA6 layer during biaxial drawing, without drastic incidence on the mechanical behavior of the multilayer films that obey a mixture law of the components, within the experimental accuracy.

The nature of the chain interactions at the layer interface deserves some comment regarding its suspected beneficial incidence on biaxial drawing. Worth mentioning is the meticulous investigation by Leger and coworkers [43–45] of interfacial adhesion and structure of polypropylene/polyamide6 bilayer cast films in which the polypropylene (PP) was blended with maleic-anhydrade-grafted polypropylene. Interfacial adhesion was shown to increase

with the density of chemical bonding between the PP-modified species and the chain ends of the polyamide6 layer. The trans-crystallization of the β-crystal form in the PP layer was ascribed to an interface-induced nucleation effect. The decrease of the crystallization temperature of the PP component in the bilayer systems as compared with the pure PP material was a strong support to the hypothesis of PP promoted nucleation. The polyamide6 layer also displayed a surprising texturing of the (002) H-bonded sheets parallel to the interface [45] that could be assigned to minimizing interfacial interactions with the PP molten layer at the moment of the polyamide6 crystallization.

In the present study which involves a much shorter contact time of the two layers in the molten state during the extrusion process (*i.e.* a few tens of seconds as compared with several minutes for the above-mentioned study), the temperature of the process was significantly higher, allowing for better reactivity between the maleic-anhydride groups of the tie layer and the amine end-groups of PA6. Besides, although good compatibility is expected between the PE and PE-*g*-MA chain species, the sandwiched tie layer directly in contact with the PA6 layer provides a much higher concentration of reactive species than in the above-mentioned study. This is thoroughly supported by the fact that none of the multilayer films could be peeled apart without involving severe plastic drawing of the PE layer whereas PA6/PE bilayer films blow-extruded without tie layer could be easily separated without any plastic deformation. However, not any signs of nucleating effect have been observed, may be due to the very fast cooling conditions that are suspected to control the crystallization kinetics over the structural factors.

The delay in the β–α strain-induced phase transition together with the chain orientation behavior of PA6 in the multilayer films under biaxial drawing are evidences that the activation of the plastic processes in the PA6 crystalline phase is somewhat modified by the presence of the PE layer. This PE effect is noticeably beneficial regarding the biaxial drawability of PA6 that is improved far beyond its capability when drawn alone. If the biaxial strain at break is highly sensitive to the film composition, and to the draw temperature to a lesser extent, a common feature to monolayer and multilayer films is yet the limiting value of the α-crystal content in the PA6 layer at break, $\chi_\alpha \approx 30\%$. In a previous study by infrared dichroism of the uniaxial drawing of neat PA6 at 100 °C [46], a similar limiting value $\chi_\alpha \approx 30\%$ was observed at the breaking strain $\epsilon \approx 2.2$. These findings suggest that the PA6 rupture occurs at a critical value of the α-phase content.

It must be pointed out that the global crystal weight fraction of the PA6 component in the blown films is only about 30% (Table 4). Besides, as can be seen in Table 5 regarding the 25PA/65PE film, the PA6 crystallinity is not modified by biaxial drawing, within the accuracy of the DSC measurements. This means that the absolute value of the critical content of α-crystals does not exceed 10% at rupture, upon equibiaxial drawing.

An explanation for this singular rupture behavior of the PA6 component may be proposed in consideration of the specific mechanical behavior of the α- and β-crystal forms [37]. The former is stiffer and less ductile than the later. Moreover, a typical feature of the α-crystal form is the strong mechanical anisotropy of the sheet-like structure having strong intra-sheet H-bonds and weak van der Waals interactions between the sheets. In the case of ethylene/vinyl-alcohol copolymers [47,48], this kind of anisotropy was shown to be responsible for a crystal cleavage propensity that is suspected to also apply to the nylon6 α-form [37]. Therefore, the strain-induced development of crack-prone α-crystals is likely to reach a critical level for crack percolation that will trigger catastrophic flaw and failure.

One may wonder about the mechanism of crack propagation for which two different routes may be envisioned. It may arise from the percolation of the strain-induced α-crystals when this stiff component reaches the geometrical percolation threshold, which is theoretically about 20% [49]. In that case, a catastrophic flaw would directly develop through the percolating crack-prone α-phase. The actual α-crystal content of about 10% in the PA6 layer seems far below the percolation threshold, but the oriented strain-induced crystallization may promote an early crystal percolation due to the form factor of the crystalline entities extending themselves in the film plane. Alternatively, the latent damage that may gradually develop in the individual crack-prone α-crystals would turn into catastrophic crack when the α-crystals are close enough to each other to enable crack percolation, before actual percolation of the α-phase.

Table 5
Crystal weight fraction of the PA6 component in the 25PA/65PE film as a function of equibiaxial strain.

Strain $\varepsilon_1 = \varepsilon_2$	0.3	1.0	1.4
Xc PA6 (%)	26 ± 3	26 ± 3	28 ± 3

5. Concluding remarks

The orientational and structural behavior of both PE and PA6 in the multilayer films is only little modified by biaxial drawing with respect to the monolayer parent films. In parallel, the stress–strain behavior of the multilayer films is not far from a simple additive mixture law of the component stress–strain curves. Nonetheless, the plastic behavior at yield of the PA6 component turned out more homogeneous in the multilayer films than in the monolayer PA6 film that develops plastic instabilities. Besides, the limiting drawability of the PA6 component is largely improved in the multilayer films: the higher the PE content, the stronger the benefiting effect on the PA6 drawability. The PE layer acts as a "deformation guide" that noticeably inhibits the PA6 propensity for plastic instability. This is suspected to result from the covalent bonding of the PE-*g*-MA tie layer that brings about strain-hardening at the PE/PA6 interfacial region. By reducing the occurrence of high local plastic deformations that generally trigger early rupture of PA6, the decrease of the PA6/PE thickness ratio results in better drawability of the PA6 layer in the multilayer films with respect to the monolayer parent.

The orientation and structure evolutions of the multilayer films do not follow those of the monolayer parent films. Quantitative analyses of the β–α phase transition and crystalline orientation of the PA6 component as a function of strain reveals significant departure between multilayer and monolayer film for $\epsilon > 0.5$. The gradual orientation of the PA6 chains in the film plane is noticeably delayed in the multilayer films concomitantly to the β–α phase transformation. Nevertheless, for similar conditions, the rupture of the monolayer and multilayer films occurs when the same relative α-crystal concentration $\chi_\alpha \approx 30\%$ is reached irrespective of the PA/PE ratio, *i.e.* about 10% of absolute α-crystal content in the PA6 component. This suggests that the PA6 film rupture is governed by a critical phenomenon in relation to the α-phase content in the PA6 layer. This critical phenomenon is ascribed to the percolation of cracks initiated in the crack-prone α-crystallites which gradually develop with increasing biaxial strain as a result of the strain-induced β–α transition.

Acknowledgements

The authors are indebted to V. Hervais and J.-M. Coillot for valuable assistance in the film manufacturing. The authors are also grateful to the Region Nord/Pas-de-Calais (ARCir program) and to the European FEDER for funding contribution to the blow-extrusion line (Ecole des Mines de Douai) and to the AFM and X-ray equipments (Université de Lille1). DSM Research (Geleen, The Netherland) is

gratefully acknowledged for providing the polyamide6 and the maleic-anhydride-grafted polyethylene of the study.

References

[1] Masuda M. In: Finch CA, editor. Polyvinyl alcohol developments. New York: Wiley; 1992. chapter. 12.
[2] Takashige M, Kanai T. Int Polym Proc 1990;5:287–91.
[3] Rhee S, White JL. Polym Eng Sci 1999;39:1160–75.
[4] Williams JCL, Watson SJ, Boydell P. In: Kohan MI, editor. Nylon plastics handbook. Munich: Carl Hanser Verlag; 1995. chapter. 10.
[5] Murthy NS. Polym Commun 1991;32:301–5.
[6] Murthy NS, Curran SA, Aharoni SM, Minor H. Macromolecules 1991;24:3215–20.
[7] Vasanthan N, Salem DR. J Polym Sci Polym Phys 2001;39:536–47.
[8] Penel–Pierron L, Debecker C, Seguela R, Lefebvre J.- M. J Polym Sci Polym Phys 2001;39:484–95.
[9] Ito M, Mizuochi K, Kanamoto T. Polymer 1998;39:4593–8.
[10] Poisson C, Hervais V, Lacrampe M-F, Krawczak P. J Appl Polym Sci 2006;101: 118–27.
[11] Wunderlich B. Macromolecular physics, crystal melting, vol. 3. New York: Academic Press; 1980. chapter.8.
[12] Rotter G, Ishida H. J Polym Sci Polym Phys 1992;30:489–95.
[13] Sibilia JP. J Polym Sci Polym Phys 1971;9:27–42.
[14] Fina LJ, Koenig JL. J Polym Sci Polym Phys 1986;24:2509–24.
[15] Yu HH, Fina LJ. Macromolecules 1994;27:6192–200.
[16] Zhang XM, Elkoun S, Ajji A, Huneault MA. Polymer 2004;45:217–29.
[17] Cole KC, Debecker C, Jutigny M, Lefebvre J-M, Krawczak P. Polym Eng Sci 2004; 44:231–40.
[18] Loo LS, Gleason KK. Macromolecules 2003;36:6114–26.
[19] Loo LS, Gleason KK. Polymer 2004;45:5933–9.
[20] Pflüger R. In: Brandrup J, Immergut EH, editors. Polymer handbook. 3rd ed. New York: Wiley-Interscience Pub.; 1989. p.V/113.
[21] Persyn O, Miri V, Lefebvre JM, Debecker C, Gors C, Stroeks A. Polym Eng Sci 2004;44:261–71.
[22] Arimoto H, Ishibashi M, Hirai M, Chatani Y. J Polym Sci Polym Chem 1965;3: 317–26.
[23] Stepaniak RF, Garton A, Carlsson DJ, Wiles DM. J Polym Sci Polym Phys 1979; 17:987–99.
[24] Read BE, Stein RS. Macromolecules 1968;1:116–26.
[25] Ferreiro V, Coulon G. J Polym Sci Polym Phys 2004;42:687–701.
[26] Kyotani M, Mitsuhashi S. J Polym Sci Polym Phys 1972;10:1497–508.
[27] Ergungor Z, Cakmak M. Macromol Symp 2002;185:259–76.
[28] Medellin–Rodriguez FJ, Larios–Lopez L, Zapata–Espinoza A, Davalos–Montoya O, Phillips PJ, Lin JS. Macromolecules 2004;37:1799–809.
[29] Yalcin B, Cakmak M. Polymer 2004;45:2691–710.
[30] Hiramatsu N, Haragushi K, Hirakawa S. Jpn J Appl Phys: Part1 1983;22:335–9.
[31] Khanna YP. Macromolecules 1991;25:3298–300.
[32] Rhee S, White JL. Polymer 2002;43:5903–14.
[33] Schouterden P, Vandermarliere M, Riekel C, Koch MHJ, Groeninckx G, Reynaers H. Macromolecules 1989;22:237–44.
[34] Mathot VBF, Pijpers MFJ. J Appl Polym Sci 1990;39:979–94.
[35] Hosoda S, Uemura A. Polym J 1992;24:939–49.
[36] Hull D, Clyne TW. An introduction to composite materials. 2nd ed. Cambridge University Press; 1996. chapter. 4.
[37] Penel-Pierron L, Seguela R, Lefebvre J-M, Miri V, Debecker C, Jutigny M, et al. J Polym Sci Polym Phys 2001;39:1224–36.
[38] Persyn O, Miri V, Lefebvre J-M, Ferreiro V, Brink T, Stroeks A. J Polym Sci Polym Phys 2006;44:1690–701.
[39] Lin L, Argon AS. Macromolecules 1992;25:4011–24.
[40] Ferreiro V, Debecker C, Laureyns J, Coulon G. Polymer 2004;45:6013–26.
[41] Schlund B, Utracki LA. Polym Eng Sci. 1987;27:380–6.
[42] (a) Kim Y-M, Park J-K. J Appl Polym Sci 1996;61:2315–24;
(b) Kim Y-M, Kim CH, Park J-K, Lee C-W, Min T-I. J Appl Polym Sci 1997;63: 289–99.
[43] Boucher E, Folkers JP, Creton C, Hervet H, Leger L. Macromolecules 1997;30: 2102–9.
[44] Laurens C, Ober R, Creton C, Leger L. Macromolecules 2001;34:2932–6.
[45] Laurens C, Ober R, Creton C, Leger L. Macromolecules 2004;37:6806–13.
[46] Miri M, Persyn O, Lefebvre J-M, Seguela R, Stroeks A. Polymer 2007;48:5080–7.
[47] Djezzar K, Penel L, Lefebvre J-M, Seguela R, Germain Y. Polymer 1998;39:3945–53.
[48] Seguela R, Djezzar K, Penel L, Lefebvre J-M, Germain Y. Polymer 1998;40:47–52.
[49] Stauffer D. Introduction to percolation theory. London: Taylor and Francis; 1985.